Non-tidal oceanographic fluctuation characteristics recorded in DONET ocean-bottom pressure time series using principal component analysis

Hideto Otsuka[1], Yusaku Ohta[1], Ryota Hino[1], Tatsuya Kubota[2], Daisuke Inazu[3], Tomohiro Inoue[4], and Narumi Takahashi[2,5]

[1]Graduate School of Science, Tohoku University, Sendai, Japan

[2]National Research Institute for Earth Science and Disaster Resilience, Tsukuba, Japan

[3]Department of Marine Resources and Energy, Tokyo University of Marine Science and Technology, Tokyo, Japan

[4]Graduate School of Science, Kyoto University, Kyoto, Japan

[5]Research and Development Center for Earthquake and Tsunami, Japan Agency for Marine-Earth Science and Technology, Yokohama, Japan

Corresponding author: Hideto Otsuka (hideto.otsuka.q6@dc.tohoku.ac.jp)

Key Points:

- We applied a principal component analysis to the long-term continuous data from a dense and wide ocean bottom pressure gauge network
- Our principal component analysis revealed the spatiotemporal characteristics of the meandering of the ocean geostrophic currents
- We propose a method to discriminate the transient tectonic signal from the bottom pressure data based on amplitudes of principal component

Abstract

Ocean bottom pressure-gauge (OBP) records play an important role in seafloor geodesy, but oceanographic fluctuations in OBP data are a major source of noise in seafloor transient crustal deformation observations, including slow slip events (SSEs), so it is important to evaluate them properly. To extract the significant characteristics of the oceanographic fluctuations, we applied principal component analysis (PCA) to the 3-year Dense Oceanfloor Network System for Earthquakes and Tsunamis (DONET) OBP time series for 40 stations during 2016–2019. PCA can separate several oceanographic signals based on the characteristics of their spatial distributions, although transient tectonic signals could not be clearly confirmed from the observed pressure records. The higher-order modes of the principal component reflected the oceanographic variation along the sea depth, and we interpreted that they were caused by the strength or weakness and meandering of ocean geostrophic currents, based on a comparison to the global ocean model ECCO2 by "Estimating the Circulation and Climate of the Ocean" (ECCO) consortium. In addition, to evaluate the ability of PCA to separate transient crustal deformation from oceanographic fluctuations, we conducted a synthetic test assuming an SSE by rectangular faults. The assumed synthetic tectonic signal can be separated from the oceanographic signals and included in the principal component independently depending on its amplitude. We proposed a transient event-detection method based on the spatial distribution variation of a specific principal component with or without a tectonic signal. This method can detect transient tectonic signals larger than moment-magnitude scale M_W 5.9 from OBP records.

Plain Language Summary

Measurement of water pressure at the seafloor can be used to detect crustal deformation in the vertical direction. This technique is extremely important for understanding various crustal deformations associated with earthquakes. To capture water pressure changes caused by crustal deformation with high accuracy; however, it is necessary to remove the water pressure changes due to ocean water. In this study, we attempted to separate these oceanic components by applying principal component analysis (PCA) to seafloor-pressure gauge data from DONET, a cable-based seafloor observation network deployed in southwestern Japan. As a result, PCA succeeded in separating multiple spatially characterized components. The higher-order modes of the principal component reflected the oceanographic variation along the sea depth, and we interpreted that they were caused by the strength or weakness and meandering of ocean geostrophic currents compared to the global model. In addition, numerical experiments were conducted to understand whether crustal deformation caused by a transient fault-slip phenomenon, called as a slow slip event, can be separated by PCA. The assumed synthetic tectonic signal can be separated from ocean-origin components. Furthermore, we propose a transient event-detection method based on the spatial distribution variation of a specific principal component with or without a tectonic signal.

1 Introduction

Seafloor geodetic observations are critical for accurately understanding crustal deformation associated with phenomena such as transient fault slips (e.g., Bürgmann & Chadwell, 2014). Among those seafloor geodetic instruments, the ocean bottom pressure-gauge

(OBP) is a sensor that can continuously observe vertical crustal deformation of the seafloor and tsunamis over a broad range of time scales and has been the subject of many previous studies (Transient crustal deformation: e.g., Ito et al., 2013; Ohta et al., 2012; Wallace et al., 2016; Suzuki et al., 2016; Sato et al., 2017; Fukao et al., 2021; Woods et al., 2022; Tsunamis: e.g., Tsushima et al., 2012; Kubota et al., 2021). However, the water-pressure time series obtained by the OBP includes various components such as tidal impacts, instrumental drift, non-tidal oceanographic fluctuations, and crustal deformation, so addressing these influences is extremely important for extracting objective crustal deformation components. Particularly, the non-tidal oceanographic fluctuation component has a characteristic time constant of more than a few days (e.g., Dobashi & Inazu, 2021), and the time constants are similar to those of slow slip events (SSEs), resulting in transient crustal deformation events (e.g., Obara & Kato, 2016; Rousset et al., 2017; Okada et al., 2022; Takagi et al., 2017). Thus, appropriate estimation and removal of non-tidal oceanographic fluctuation components are critical for the accurate identification of the tectonic components. Such non-tidal oceanographic components can be removed by applying a bandpass filter to eliminate oceanic origins, excluding specific constants (Sato et al., 2017; Wallace et al., 2016; Suzuki et al., 2016; Muramoto et al., 2019), and using a physical model to calculate the expected pressure fluctuation values and remove them from the observed time series (Inazu et al., 2012; Dobashi & Inazu, 2021). Although these methods can improve the signal-to-noise ratio of non-tidal oceanographic fluctuations, their spatiotemporal characterization is required to enable smaller tectonic-induced pressure changes detection.

The spatiotemporal characteristics of these non-tidal oceanographic components recorded in the OBP have been identified in several previous studies. Muramoto et al. (2019) found that the oceanographic fluctuations recorded in the OBP time series off Hikurangi, New Zealand [Hikurangi Ocean Bottom Investigation of Tremor and Slow Slip (HOBITSS), which extends ~60km square; e.g., Wallace et al., 2016], became less similar as the difference in sea depth between OBP sites increased. Inoue et al. (2021) used the standard deviation of the relative pressure time series between stations in the same observational network and observation period as Muramoto et al. (2019), to evaluate the station distance and sea-depth difference in the similarity of the time series. These studies showed that the depth dependence was more significant than the station-distance dependence in the OBP time series. However, the larger spatial characteristics of these non-tidal oceanographic fluctuation components still need to be investigated. The current interpretations and discussions of the similarity of these features at similar sea-depths are also insufficient.

Principal component analysis (PCA) (e.g., Jolliffe, 2002) is a standard technique for analyzing large datasets containing a high number of dimensions/features per observation, increasing the interpretability of data while preserving the maximum amount of information. PCA has been employed in land-based geodesy (e.g., Munekane, 2012; Kositsky & Avouac, 2010), seafloor geodesy (e.g., Hino et al., 2014; Gomberg et al., 2019), oceanography (e.g., Kundu et al., 1975; Kutzbach, 1967; Androsov et al., 2020), and other fields to evaluate and remove common modes. Hino et al. (2014) applied PCA to the OBP time series and showed that it could remove non-tidal oceanographic fluctuation components common to the entire OBP network. They demonstrated that the signal-to-noise ratio of the OBP time series could be improved by removing the first principal component (PC). Watts et al. (2021) applied Complex PCA (Thomson & Emery, 2014; Nuryanto, 2016), which can also evaluate propagation components by extending PCA to complex numbers, to four OBP time series stations and evaluated its performance with respect to removing oceanographic components from the OBP

time series. These previous studies have already shown that PCA effectively removes non-tidal oceanographic fluctuations from the OBP time series, but a spatiotemporal assessment of each of the extracted components is lacking.

Given this research background, this study focuses on the OBP observation network in the Dense Oceanfloor Network system for Earthquakes and Tsunamis (DONET) (Figure 1; Kaneda et al., 2015; Kawaguchi et al., 2015) in southwest Japan, where the observation network is densely and widely distributed. In the Nankai trough region, where the DONET is installed, the transient SSEs have been oftern observed and the spatiotemporal variation of the SSE activities is extensively studied (e.g., Obara & Kato, 2016; Yokota & Ishikawa, 2020). Thanks to the long-term continuous observations and the spatial extent of the DONET data, we can quantify the spatial characteristics of non-tidal oceanographic fluctuations in further detail and can evaluate the ability of PCA to separate tectonic and oceanographic signals, which have not been done in the past studies. Therefore, we apply PCA to the long-term time series of the DONET data, and examine its spatiotemporal characteristics. Furthermore, we discuss the possibility of applying PCA to data in which transient crustal deformations are included in the OBP time series to separate these features from the time series. We further propose a transient event-detection method based on the spatial distribution variation of a specific principal component.

2 Data and Principal component analysis

2.1 Seafloor pressure data and data processing

We used OBP data acquired via a cabled seismic observation system named DONET in the Nankai Trough in southwestern Japan. The DONET observatory includes an accelerometer, broadband seismometer, pressure sensor, hydrophone, thermometer, and other sensors to observe the seafloor conditions. Absolute quartz oscillation pressure sensors by Paroscientific, Inc. are used as pressure sensors, with a sampling frequency of 10 Hz (Matsumoto & Araki, 2021). The DONET observatory consists of two cables (Figure 1) with several nodes, which are groups of four or five observation sites in the vicinity. The eastern cable (DONET1, KMA to KME nodes; 22 stations) began monitoring in 2011, and the western cable (DONET2, MRA to MRG nodes; 29 stations) began monitoring in 2016 (Figure 2). For example, KMA node includes the stations of KMA01–KMA04, and MRF node includes the stations of MRF22–MRF25 (Figure 2). To ensure a sufficient time-series data length, 40 sites from June 2, 2016, to August 12, 2019, with few missing measurements, were used for the analysis (red-colored sites in Figure 1). The pressure data for all the KMA sites and MRF22 were not available after October 2018 and March 2018, respectively. No data for the KME sites were available during the analysis period.

The OBP time series contains signals other than the targeted crustal deformation. The observed OBP time series can be described by Equation 1 (e.g., Ito et al., 2013; Hino et al., 2014):

$$\Delta p_B(t) = \Delta p_C(t) + \Delta p_T(t) + \Delta p_O(t) + \Delta p_D(t) + \varepsilon(t), \#(1)$$

where $\Delta p_B(t)$, $\Delta p_C(t)$, $\Delta p_T(t)$, $\Delta p_O(t)$, $\Delta p_D(t)$, and $\varepsilon(t)$ represent the observed pressure, crustal deformation, tidal signal, non-tidal oceanographic fluctuations, instrumental

drift, and other errors, respectively. The following procedure was used to extract the crustal deformation component from the OBP time series.

The original 10 Hz sampling data were down-sampled by averaging them over one hour. The missing parts were linearly interpolated to use the tide-killer filter as follows: the tidal component ($\Delta p_T(t)$) was removed using a low-pass filter designed for removing tidal components (the 48-hour tide-killer filter designed by Hanawa & Mitsudera, 1985). This tide-killer filter extended the Thompson (1983) filter to 48 h. It uses a 10-day weighted moving average to reduce the filter response factor to approximately zero in less than 2 days (for the weighting factor, see Table3 by Hanawa & Mitsudera (1985)). The weighting factors of this filter were adjusted so that the inertial motions contained in tidal currents and other oceanographic phenomena near Japan could also be removed. Bayesian Tidal Analysis Program – Grouping Model program (BAYTAP-G) (Tamura et al., 1991) is often used to estimate and remove tidal variations from OBP time series; however, small fluctuations with a high frequency (time constant of less than 2 days) remain in the time series. Here, we are interested in crustal deformation in the range of a few days or more; high-frequency variations are outside the scope of this study. Therefore, a simple low-pass filter was applied. The tide-killer filter produces inappropriate variability when applied to a time series that does not include tidal variations. Hence, the missing parts and the time series for the 5 days before and after the missing periods were removed before the instrumental drift estimation. The instrumental drift component ($\Delta p_T(t)$) was estimated and removed using linear and exponential approximations (Watts & Kontoyianiss, 1990; Polster et al., 2009); the averaged drift rate over the stations was approximately several hPa per year. The missing part of the time series was reinterpolated using a piecewise cubic Hermite interpolating polynomial (Fritsch & Carlson, 1980). Processed data, in which tectonic and oceanographic signals remained, were used in the following analyses. These processed data are called “observed data” in the sections hereafter.

2.2 Principal component analysis

We assumed that the observed data contained multiple spatially correlated non-tidal oceanographic fluctuations signals that could be separated by PCA, which is a major multivariate analysis method that uses as few synthetic variables as possible to capture as much information as possible (e.g., Jolliffe, 2002). We applied PCA to the observed data to extract non-tidal oceanographic components with spatial similarities from the OBP time series. This study first applied PCA to such a long-term OBP data set to extract non-tidal oceanographic components for extracting crustal deformation data. We adopted the conventional PCA method for the preprocessed observed data. For each extracted PC, a judgment was made on whether the component should be attributed to the non-tidal oceanographic contribution based on its spatial characteristics.

As mentioned in the introduction, a sea-depth dependence exists for the oceanographic fluctuations in the OBP data (e.g., Inoue et al., 2021). To confirm these PCA effects and the subsequent selection and removal of PCs, the relative pressure between sites in the OBP time series was calculated, and their dependence on the difference in distance and sea depth was also calculated. Differences from an assumed reference site were calculated for all sites, the standard deviation (SD) of the relative water-pressure time series at each site was determined and the dependence on distance and sea depth between those stations was evaluated. In this paper, we use the absolute averaged SD for overall stations (ASD) and the relative SD for each station

(RSD) to explain the PCA contributions shown as below. The ASD for the time series types of l is shown in Equation (2):

$$ASD^l = \frac{1}{N}\sum_{i=1}^{N}\sqrt{\frac{1}{T}\sum_{t=1}^{T}\left(P_{i,l}^t - \overline{P_{i,l}}\right)^2}, \#(2)$$

where $P_{i,l}^t$ indicates the pressure at time t at station i, and $\overline{P_{i,l}}$ denotes the temporal average of $P_{i,l}^t$. The types of $l = 1, 2, \ldots 9$ indicate the observed pressure, first PC (PC1), second PC (PC2), third PC (PC3), fourth PC (PC4), and the observed pressure after subtracting PCs 1 and 2, after subtracting PCs 1–3, after subtracting PCs 1, 2, and 4, and after subtracting PCs 1–4, respectively. The RSD at station i from the reference station j is shown in Equation (3):

$$RSD_{ij}^l = \sqrt{\frac{1}{T}\sum_{t=1}^{T}\left\{\left(P_{i,l}^t - P_{j,l}^t\right) - \left(\overline{P_{i,l} - P_{j,l}}\right)\right\}^2}, \#(3)$$

where $P_t^{i,l}$ and $P_t^{j,l}$ indicate the pressure record at time t at station i and j, respectively. $\overline{P_{i,l} - P_{j,l}}$ denotes the average of the relative pressure time series between station i and j.

3. Results

Figure 2 shows example of the OBP time series after removing the tidal and drift components from the observed time series. These time series show annual variations: a higher pressure value appeared in the summer season (July to August) and a lower pressure value appeared in the winter season (January to February). This annual variation is evident even before 2016 in DONET1 network, which is outside of the period of our analysis (KMB–KMD time series in Figure 2). The annual variation has an amplitude of up to 5 hPa, and these characteristics are within the same node and display similar features over a wide area. Similar characteristics can be observed throughout the network, even for shorter time-constant variations. In the following sections, we present the PCA results that separate these spatially coherent oceanographic fluctuations.

3.1 Spatiotemporal characteristics of each principal component

In PCA, PC1 has the largest eigenvalue. PC1 is more highly correlated with the original features than PC2, and PC2 is better correlated than the PC3, and so on. PCA reduces the dimensionality of the data by selecting the first k PCs to represent the original data. Figure 3 (a–d) shows the extracted PCs at the DONET OBP sites. The eigenvector and eigenscore of each PC correspond to its spatial distribution and temporal variation, respectively. The contributions of

each PC were 75.7% for PC1, 10.3% for PC2, 3.5% for PC3, and 2.5% for PC4 (Right top number in Figure 3). The contribution reached 92% through PC4, and the spatial patterns and other characteristics of the higher-order components after PC5 were not clear, therefore, the sections hereafter will utilize PC1–PC4 to interpret their characteristics. PC1 and PC2 explain the majority (86.0%) of the time series characteristics; PC1 is the common component across the entire observation network and includes the annual variability (Figure 3 (a) and Figure 4(a)). PC2 has a spatially inclined characteristic, reversing the positive and negative eigenvector values between the shallow and deep stations (Figure 3(b) and Figure 4(c)). This sea-depth-dependence characteristic is clear in the time series of PC2, whose amplitude is notably large in shallow or deep stations (Figure 5(b)). PC3 does not have a clear sea-depth dependency like PC2, but it does have a longitudinal dependence characteristic (Figure 3(c) and Figure 4(f)). PC4 has parabolic spatial characteristics with positive and negative eigenvector values at shallow and deep water depths, respectively (Figure 3(d) and Figure 4(g)). Based on the characteristics of each of these PCs, PCs 1–4 were determined to be the components that needed to be removed from the oceanographic fluctuation components in this study.

Previous studies have noted the sea-depth dependency of the seafloor water-pressure characteristics based on actual observation data and oceanographic models (e.g., Inoue et al., 2021; Fredrickson et al., 2019). The PCA results obtained in this study were consistent with the those obtained in previous studies. The results also suggest that not only can the depth-dependent component be extracted as the main component, but it can also be separated into two different components: PC2 and PC4.

3.2 Contribution of the principal components in the OBP time series

To confirm how the noise in the OBP time series can be reduced using the extracted PCs, the results of subtracting the PCs from the original observed data in different combinations are shown in Figure 6. After removing PC1 (Figure 5(a)), which includes the annual variation component, the ASD of the time series was considerably reduced from 1.98 hPa to 0.91 hPa (the ASD value was reduced by 46%), while the spatially correlated variations remained (Figure 6 (b)). The characteristics of the remaining components are not common to the entire observation network but are identified at specific sites, which suggests that they reflect depth-dependent oceanographic fluctuations. Figure 6(c) shows the results obtained by subtracting PC1 and PC2 from observed data. In Figure 6(b), the remaining variation was eliminated, and the ASD has decreased to 0.69 hPa (the ASD value was further reduced by 24%, for an overall reduction of 65%). Removing PCs 1–3, the ASD decreased to 0.61 hPa (Figure S1(b)), and removing PCs 1, 2, and 4 resulted in an ASD of 0.62 hPa (Figure S1(c)). Finally, removing PCs 1–4 resulted in an ASD of 0.53 hPa (Figure S1(d)), reducing the noise level by 73% compared to the time series before the PCs were removed. PCA is a method of identifying as much information as possible using as few synthetic variables as possible. Naturally, subtracting the principal components with high contributions from the original data reduces their noise levels; however, as previously mentioned, PCs 1–4 showed distinct spatially correlated variations that could be attributed to oceanic origins. Therefore, subtracting these PCs appeared to be a reasonable procedure. In particular, PC1 and PC2 reflected most of the common or depth-dependent gradients of oceanographic fluctuations in the OBP time series, because the sum contributions of both reached 86.0%, and the sum contributions of PC3 and PC4, which also reflect the oceanic signal, were only 6.0% (Figure 4). These results also suggest that PCA can efficiently remove depth-dependent oceanographic fluctuations, as indicated in previous studies (Muramoto et al., 2019;

Inoue et al., 2021; Fredrickson et al., 2019). In addition, reducing the noise level via pressure values at individual sites rather than calculating the pressure differences between sites is considered a significant advantage. In the next section, we confirm more detail the extent to which the PCA removes these depth-dependent oceanographic fluctuations.

3.3 Reduction of sea-depth dependency based on PCA

As mentioned in the introduction, Inoue et al. (2021) found that the characteristics of oceanographic fluctuations depend on sea depth. In this section, we quantitatively discuss the extent to which these depth dependencies are reduced by PCA, as described in the previous sections. First, we calculated the relative pressure time series for all the stations used in the analysis. Next, the RSDs were calculated and plotted as a function of the difference in depth or distance between sites. Similar calculations were applied to the results obtained in the previous section by subtracting the PCs to confirm their characteristics. In addition, correlation coefficients were calculated to quantitatively evaluate the dependence.

Figure 7(a–b) shows the sea depth and distance dependency, respectively, before PCA was applied to the time series. The results for Hikurangi, New Zealand, by Inoue et al. (2021) are also included for comparison (red dots in Figure 7(a–b)). This figure shows that the depth dependence is more distinct than the distance dependence. This trend is also consistent with that of off-Hikurangi margin. Figure 7(c–d) shows the correlation plot when PC1 was subtracted from the original observed time series. It is interesting to note that the depth dependence visible in the original time series was not reduced. This result suggests that PC1 contains a common component throughout the observation network, which contributes little to the spatial variation of the observation data even after its influence is removed. The results of subtracting PC1 and PC2 are shown in Figure 7(e–f), which indicates that subtracting PC2 significantly reduced the dependence on sea depth. The correlation coefficient when only PC1 was subtracted was 0.78, which was almost halved to 0.40 when both PC1 and PC2 were subtracted. Interestingly, for distance dependence, the ASD itself decreases significantly (from 0.91 to 0.69), although the value of the correlation coefficient itself does not change significantly (from 0.35 to 0.30). This suggests that PC2 can adequately remove only the sea-depth-dependent component of the OBP time series. The fact that the DONET observation network has a slightly elongated shape in the direction of the isobaths (Figure 1) also helps ensure that the removal of the sea depth dependence does not reduce the distance dependence. Figure S2(e–f) shows the results obtained after subtracting PCs 1, 2, and 4. Consequently, the depth dependence was further reduced with a correlation coefficient of 0.33, approximately 60% smaller than that of the original time series. However, Figure S2(c–d) shows the result after subtracting PCs 1–3. PC3 does not reduce the sea depth dependence (from 0.40 to 0.40), although it contributes slightly to reducing the distance dependence (from 0.30 to 0.26). After removing PCs 1, 2, and 4 or PCs 1–4, the correlation coefficient of the sea-depth dependence is almost equivalent to the distance dependence, indicating that removing PCs 1, 2, and 4 can significantly reduce the depth dependence of oceanographic fluctuations.

Previous studies have noted that applying PCA may reduce the detection accuracy of crustal deformation owing to the seepage of crustal deformation components into the principal components (Watts et al., 2021). Therefore, in the next section, we discuss the accuracy of crustal deformation detection by PCA using synthetic rectangular faults in the observation region.

4 Discussion

4.1 Physical oceanographic interpretation of each principal component

In the previous section, PCA was used to successfully extract components with multiple spatial characteristics. The observed pressure time series include both oceanographic fluctuations and tectonic signals but the oceanographic circulation models include only the oceanographic fluctuations. To examine the characteristics of oceanographic fluctuations, we applied PCA to ocean models and compared the spatial distribution of each PC with the observation. The ocean models have advantages and disadvantages in the region and time scale used herein, depending on the input data and model structure (Dobashi & Inazu, 2021). We chose a single-layer ocean model (SOM) (Inazu et al., 2012) and ECCO2 (Menemenlis et al., 2008) for comparison with observations. SOM assumes a single-layer barotropic ocean model and is driven by atmospheric pressure as well as wind stress, whereas ECCO2 assumes a multiple-layer (50 layers) baroclinic ocean model (i.e., better vertical resolution than SOM) and is driven by wind stress, heat, and freshwater flux although the atmospheric pressure is not considered. The details of each model are referenced in Table 2 by Dobashi & Inazu (2021). The expected pressure time series was calculated based on each model. As each numerical model provides calculations for each grid, the grid nearest to the DONET observation region (77 grids in longitude of 134°E–137°E and latitude of 32°N–34°N) was selected, and PCA was applied to the time series data to confirm the characteristics of the model.

After applying PCA to SOM, the PC1 contribution reached 96.7% (Figure S3(a)). This is clearly larger than the 75.7% observed (Figure 3), indicating that ocean variations show similar fluctuations (Figure S3). Overall, the pressure variation due to the oceanographic fluctuations is expressed, but the contribution is more exaggerated than the observation. In contrast, higher-order terms, such as the sea-depth-dependent component identified in the observational data, were poorly extracted from the SOM. Importantly, when applying PCA to ECCO2, PC1, PC2, PC3, and PC4 contributed 80.8%, 9.9%, 2.9%, and 1.8%, respectively. The contribution ratio and the spatial distribution (Figure S6) were similar to the observational data (Figure 3). The reproduced oceanographic fluctuations calculated by ECCO2 are more realistic than SOM.

The extracted PC characteristics of ECCO2 were as follows. PC1 was the overall pressure variation with a large spatial scale (several hundred km extent) driven by wind stress and atmospheric pressure, which was also reproduced by SOM. PC2 was the depth-dependent component (i.e., a pattern orthogonal to isobath). PC3 and PC4 were the depth-dependent patterns but their frequency was higher than PC2 (Figure S6; Figure S8). The longitudinal dependence component seen in PC3 of the observed data is part of the parabolic component seen in PC3 or PC4 of ECCO2 and is considered to be included in these components.

Following confirmation that the PCs extracted from the observed time series were due to oceanographic fluctuations, we attempted to interpret them qualitatively. The Nankai Trough, where DONET stations are installed, is a channel of the Kuroshio Current (e.g., Nitani, 1972), which meanders widely on time scales of several years or more (e.g., Kawabe, 1985). For example, one of the largest Kuroshio meanders occurred in 2017 and continued through 2022, contributing to pressure fluctuations on the seafloor (Nagano et al., 2019; 2021). Therefore, oceanographic phenomena such as the strength and meandering of the Kuroshio Current should be recorded in the OBP data for the DONET region. The meandering of the geostrophic current including Kuroshio is interrelated with the mesoscale eddy (Qiu & Miao, 2000; Hasegawa et al.,

2019) with ~100 km radius and their contribution to the sea bottom pressure perturbation cannot be well separated. Note that the sea level variation due to the meso-scale eddies is considerably attenuated to the ocean bottom pressure variation because the sub-seasurface water column imperfectly compensates for the pressure change by seasurface variation (Dobashi & Inazu, 2021; Hasegawa et al., 2021).

Based on the results of the application of PCA to the observed data and ocean models and the previous studies on oceanographic fluctuations and the Kuroshio Current (Hasegawa et al., 2021), we interpreted each PC in the observed data as follows. PC1 is the large spatial scale variation associated with wind stress and atmospheric pressure variation. PC2 corresponds to the strength and weakness and flow axis position of the geostrophic current (e.g., Kuroshio Current) (Figure 8(a)). Both PC3 and PC4 can be compatible with the spatial pattern depending on the location of the mesoscale eddy, which has a radius of fewer than 50km (Figure 8(b, c)). If the centroid of the cold vortex is located east (Figure 8(b)) or west (Figure 8(c)) of the Kii Peninsula, the longitudinal dependence variation can reflect in the observed data in DONET. When the cold vortex migrates eastward or westward orthogonally to the direction of isobath (i.e., changes from Figure 8(b) to (c) or Figure 8(c) to (b)), a parabolic-like spatial distribution can occur. As mentioned above, the sea-surface level fluctuations are not directly reflected as seafloor pressure variations, but fluctuations caused by mesoscale eddies are thought to affect ocean bottom pressure.

In this analysis, PCA was applied to a long-term continuous time series of more than 3 years. However, if the components reflected in the principal components have characteristic time constants, changing the time window may change the extracted components. Nevertheless, applying PCA to the OBP time series shows that pressure fluctuations of oceanic origin can be separated based on their spatial characteristics. This suggests that the method can improve the data quality in time series when extracting pressure variations caused by crustal deformation. In the next section, we discuss the potential usefulness of PCA when transient crustal deformations are included in a time series.

4.2 Synthetic test for principal component analysis to observe the crustal deformation

As shown in the previous section, applying PCA to the DONET time series can separate the non-tidal oceanographic fluctuations in the observed data; PC2 and PC4 could explain the most depth-dependent oceanographic fluctuations in the OBP time series. In contrast, it is necessary to evaluate the ability of PCA to separate transient tectonic and oceanographic signals to improve the reliability of crustal deformation observations using OBPs. Watts et al. (2021) performed a Complex PCA after adding a synthetic ramp function to the OBP time series of four stations and found that part of the ramp signal interfered with the principal component, which mainly reflects oceanographic fluctuations. This result suggests that subtracting the oceanographic component from the observed time series also removes part of the tectonic signal and may underestimate the amplitude of the displacement caused by the transient event. In this section, we evaluate the possibility of separating tectonic and oceanographic signals by applying PCA to the OBP time series.

4.2.1 Analytical overview of the synthetic test

In this section, we describe how to add a synthetic signal to the OBP time series. A rectangular fault model (Okada, 1992) was used. The results were assumed for each earthquake

moment magnitude (M_W 5.5–7.0, 0.1 increments) based on the scaling law proposed by Wells & Coppersmith (1994). The rigidity and Posson's ratio were assumed for 30GPa and 0.25, respectively. The fault locations were set along the plate boundary of the Phillippine Sea plate (Baba et al., 2002; Hirose et al., 2008; Iwasaki et al., 2015). The strike, dip, and rake angles of the fault were assumed to be 250°, 8°, and 90°, respectively, assuming a reverse fault along the plate boundary. The assumed fault model was horizontally spaced at 0.1° intervals. Figure S9 shows the centroid of all 548 fault planes. For each assumed fault model, the time evolution of the fault slip was calculated using a ramp function based on the duration and total amount of slip expected from the moment magnitude. The duration of an SSE is estimated as in Equation (4), following the scaling law between the magnitude and duration estimated by the observed slow earthquakes (Ide et al., 2007):

$$Mo \sim T \times 10^{12-13}, \#(4)$$

where Mo indicates the seismic moment [N m] and T indicates the duration period [s]. In this study, we calculated the value of the duration T using the observed SSE parameter around the Kii Peninsula investigated by Sekine et al. (2010), which is written as follows:

$$Mo = T \times 10^{12.2}. \#(5)$$

Table 1 shows the duration, length of the rectangular faults, and other parameters at representative magnitudes calculated based on the results of Wells & Coppersmith (1994) and Equation (5). The timing of the synthetic ramp application was set so that the center of the lamp coincided with the middle of the entire observation period (January 1st, 2018).

4.2.2 Extraction of transient crustal deformation by PCA

A ramp function with an amplitude duration corresponding to the fault position and earthquake size was added to the observed OBP time series. PCA was applied to investigate how the components that responded to the ramp function were affected by the principal components. The OBP time series expected by the M_W7.0 event at 135.5°E and 33.0°N is shown in Figure 9(a), and the spatial distribution of seafloor vertical displacement and each PC is shown in Figures 10(b–f). In this case, the vertical displacement at the station reached a 20.1 cm uplift (20.1 hPa pressure decrease) at station MRE21 (Figure 9(b)). The vertical displacement associated with SSE was extracted as PC1. The common, depth-dependent, and longitude-dependent components were extracted from PCs 2, 3, 4, and 5, respectively (Figures 10(c–f)). On the other hand, when the M_W6.7 event at the same location fault was assumed, a PC including the assumed ramp function was classified into PCs 1 and 2 (Figure 10(b) and (c)). PCs 1 and 2 also included the common components, and PCs 3–5 includes depth-dependent and longitude-dependent components (Figure 10(d–f)). The assumed ramp and common components were mixed in PCs 1 and 2 because of their similar amplitude; the contribution of PC1 and PC2 were 53.1% and 35.6%, respectively. This result indicates that principal components were shifted to higher-order modes by one before displacement by the SSE was added, for each. In this example,

the expected displacements were sufficiently large compared to the accuracy of the OBP observations, which were classified as PC1. Figure 11 illustrates the principal components extracted for each component as the earthquake magnitude was reduced for the same fault location. From this figure, it can be observed that the displacement field expected by the SSE gradually shifts to a higher-order mode.

These results suggest that PCA can be applied to the time series of transient crustal deformations caused by SSE to extract those tectonic signals as principal components along with oceanographic fluctuations. Thus, the principal components of the time series include transient crustal deformation and those do not include the deformation can be compared; in other words, if the difference between their spatial distributions (each eigenvector element) is significant, they can be extracted. In subsequent sections, we propose a method for evaluating crustal deformation using the spatial distribution of PCs estimated by PCA and evaluate its effectiveness.

4.2.3 Evaluation of spatial characteristics

We used the absolute value of the normalized inner product (NIP) of the eigenvectors to estimate the spatial characteristics of the results extracted using PCA. The amplitude of each OBP site for each PC corresponded to each element of the eigenvector PC. The NIP of two eigenvectors of the same value is 1; if the difference between them is large, the value is close to 0. When the amplitude of the OBP time series due to crustal deformation is smaller, crustal deformation signals and oceanographic fluctuations may be mixed in the same PC. Figure S10 shows the spatial distribution of PC2 for each magnitude, assuming a rectangular fault at 135.5°E, 33.0°N. This shows that if the event is small and the expected crustal deformation is classified as PC1 and/or PC2, then PC2 includes other noise components like oceanographic fluctuations. Therefore, in this section, we consider using the PC2 difference, with and without synthetic crustal deformation to improve the efficiency of crustal deformation detectors using PCA. Table 2 shows the NIP between the two PC2s without changing the fault location. In this example, if the assumed event was a fault with a magnitude of M_W6.2 or less, the crustal deformation component would be classified as PC3, in which case the NIP would be approximately 1. In other cases, the expected crustal deformation components are not separated into independent PCs and are mixed with other oceanographic fluctuations (M_W6.7 and M_W6.3 in Figure 11). For example, for M_W6.3, the NIP of PC2 was 0.78, and its spatial distribution included inclined oceanographic fluctuations and crustal deformation (Figure S10).

4.3. Comprehensive synthetic test for PCA

Based on the evaluation of spatial characteristics of the results of PCA, we conduct an analysis (assuming faults) using NIP as a proxy for each grid assuming faults, and quantitatively evaluate the magnitude of events detected by PCA. Figure 12 shows the results when 0.75 or 0.52 is used as the upper NIP limit threshold between PC2s (i.e., a change is detected when NIP < 0.75 or NIP < 0.52). The ability to detect crustal deformation is naturally higher in the neighborhood of OBP sites, and the magnitude of the moment of the lower detection limit increases with distance. On the onshore side—away from the trench axis—the plate boundary is relatively deeper, and the expected displacement is smaller, therefore, the lower detection limit for the magnitude is larger. Alternatively, land-side crustal deformations can be observed using on-land continuous GNSS (Global Navigation Satellite System) sites (e.g., GEONET; GNSS Earth Observation Network System operated by the Geospatial Information Authority of Japan

(GSI)). In addition, the Mw6–6.5 events can be detected by only on-land GNSS (Suito, 2016). The accuracy of SSE detection was also examined by integrating both on-land and seafloor observation networks (Agata et al., 2019), but this is beyond the scope of this study.

The lower limit of the event size at which crustal deformation can be detected strongly depends on the NIP threshold. Naturally, the threshold value is smaller, and the lower limit of the detectable M_W is larger (Figure S11). To decide the best NIP threshold for this analysis, we focused on the NIP variation depending on the M_W migration. The NIP changed with the M_W for each rectangular fault point: The maximum NIP change at 135.5°E, 33.0°N is 0.38 (from 0.40 to 0.78) during the M_W migration between 6.4 to 6.3 (Figure S10). Similarly, comparing the pattern of change in M_W and NIP for each rectangular fault, we found that NIP changed abruptly at each specific M_W. This suggests that the crustal deformation component clearly migrates to higher-order modes as M_W is reduced for almost all fault locations in our analysis method (Figure S11). We fixed every NIP change pattern by the largest change in NIP, and the average and standard deviation at each M_W were examined (Figure S12). In Figure S12, the largest NIP change was set as the relative M_W between 0.1 and 0.0. The NIPs above 1σ at the lower and upper side of the largest NIP change were between 0.52 and 0.75. Consequently, we propose a practical NIP threshold value be included in this range. Comparing the cases with NIP thresholds of 0.52 and 0.75, it can be seen that the lower detection limit M_W was naturally smaller for 0.75, while the overall spatial distribution was generally consistent (Figure 12). This suggests that the anomaly detection ability of our method is not significantly different when the threshold value is selected within this range. In the case of NIP threshold value of 0.75, at the rectangular fault at 136.8°E, 33.1°N, the smallest event of M_W5.9 can be detected by our detection method (Figure 12). The spatial distribution of the lower limit of the moment magnitude of a detectable event corresponds to a pressure step with an amplitude greater than one signal-to-noise ratio at five or more stations. The reason the fault at this location was on the lower limit of detection is thought to be because the assumed fault depth was relatively shallow and located near the observation point.

5 Conclusions

By applying PCA to the DONET OBP time series from 2016 to 2019, we verified the spatiotemporal characteristics of oceanographic fluctuations in the Nankai region of Japan. The oceanographic fluctuation characteristics of sea-depth dependency found by Inoue et al. (2021) appeared in the Nankai region, and were reflected in PC2 and PC4. From the spatial distribution of these principal components, we inferred that these sea-depth dependencies were caused by the strength and weakness or the meandering of ocean geostrophic currents and mesoscale eddies. Finally, we could not detect any significant transient tectonic events in the OBP time series. This suggests that the amplitude of the transient events was too small to detect, or the signal seeped into the principal components interpreted as oceanographic fluctuations.

We added synthetic ramps, assuming an SSE of moment magnitude between 5.5 and 7.0, to the observed time series to evaluate the ability of PCA to separate the tectonic and oceanic signals. The added synthetic ramp signal can be divided into independent principal components depending on their scale. We proposed a transient event-detection method using PCA applied to the OBP time series. The lower limit of the magnitude of the detectable event depends on the NIP threshold, although the M_W5.9 event can be detected from the pressure data on the rectangular fault with the best observation points. In the future, we will systematically detect

SSEs using this method and compare them with slow earthquake activity detected previously to better understand the occurrence mechanisms of slow earthquakes.

Acknowledgments

This study was supported by the Japan Science and Technology Agency (JST) Fusion Oriented Research for disruptive Science and Technology (FOREST) Program (grant number: JPMJFR202P, Japan). This study was also supported by the Ministry of Education, Culture, Sport, Science and Technology (MEXT) of Japan, under its The Second Earthquake and Volcano Hazards Observation and Research Program (Earthquake and Volcano Hazard Reduction Research). This work was also supported by the Research Project for Disaster Prevention on the great Earthquakes along the Nankai Trough by MEXT. WISE Program for Sustainability in the Dynamic Earth supported Hideto Otsuka financially. All figures in this paper was created by Generic Mapping Tools 5 (Wessel et al., 2013).

Data Availability Statement

The DONET (https://doi.org/10.17598/NIED.0008) is jointly operated by the Japan Agency for Marine-Earth Science and Technology (JAMSTEC) and the National Research Institute for Earth Science and Disaster Resilience (NIED) after April 1st, 2016, and the seafloor pressure data during this period is available with data request and permission at the website of NIED (https://hinetwww11.bosai.go.jp/auth/oc/, accessed on November 1st, 2022). DONET was operated by JAMSTEC before March 31st, 2016, and the data in this period is available at the website of JAMSTEC (https://www.jamstec.go.jp/ceat/donet_data/j/technical/ and https://join-web.jamstec.go.jp/join-portal/, accessed in 2018), but now the data access is partially suspended and inquiries are needed

(https://www.jamstec.go.jp/e/about/informations/notification_2021_maintenance.html, accessed on November 1st, 2022).

References

Agata, R., Hori, T., Ariyoshi, K., & Ichimura, T. (2019), Detectability analysis of interplate fault slips in the Nankai subduction thrust using seafloor observation instruments. *Marine Geophysical Research, 40*(4), 453-466. doi: 10.1007/s11001-019-09380-y.

Akaike, H. (1973), Information theory and an extension of the maximum likelihood principle. *2nd International Symposium on Information Theory*, eds. Petrov, B. N., and Caski, F., Akadimiai Kiado, Budapest, 267-281, https://doi.org/10.1007/978-1-4612-1694-0_15.

Androsov, A., Boebel, O., Schröter, J., Danilov, S., Macrander, A., & Ivanciu, I. (2020), Ocean bottom pressure variability: Can it be reliably modeled? *Journal of Geophysical Research: Oceans, 125*(3), e2019JC015469. doi: 10.1029/2019JC015469.

Baba, T., Tanioka, Y., Cummins, P. R., & Uhira, K. (2002), The slip distribution of the 1946 Nankai earthquake estimated from tsunami inversion using a new plate model. *Physics of the Earth Planetary Interiors, 132*(1-3), 59-73. doi: 10.1016/S0031-9201(02)00044-4.

Bürgmann, R., & Chadwell, D. (2014), Seafloor geodesy. *Annual Review of Earth and Planetary Sciences, 42*, 509-534. doi: 10.1146/annurev-earth-060313-054953.

580 Dobashi, Y., & Inazu, D. (2021), Improving detectability of seafloor deformation from bottom
581 pressure observations using numerical ocean models. *Frontiers in Earth Science: Solid Earth*
582 *Geophysics, 8*, 598270. doi: 10.3389/feart.2020.598270.
583
584 Fredrickson, E. K., Wilcock, W. S. D., Schmidt, D. A., MacCready, P., Roland, E., Kurapov, A.
585 L., et al. (2019), Optimizing seafloor configurations for the detection of slow-slip earthquakes in
586 seafloor pressure records, using the Cascadia subduction zone as a case study. *Journal of*
587 *Geophysical Research: Solid Earth, 124*(12), 13,504-13,531. doi: 10.1029/2019JB018053.
588
589 Fritsch, F. N., & Carlson, R. E., (1980), Monotone piecewise cubic interpolation. *SIAM Journal*
590 *on Numerical Analysis, 17*(2), 238-246. doi: 10.1137/0717021.
591
592 Fukao, Y., Kubota, T., Sugioka, H., Ito, A., Tonegawa, T., Shiobara, H., et al. (2021), Detection
593 of "rapid" aseismic slip at the Izu-Bonin Trench. *Journal of Geophysical Research: Solid Earth,*
594 *126*(9), e2021JB022132. doi: 10.1029/2021JB022132.
595
596 Gomberg, J., Hautala, S., Johnson, P., & Chiswell, S. (2019), Separating sea and slow slip
597 signals on the seafloor. *Journal of Geophysical Research: Solid Earth, 124*(12), 13,486-13,503,
598 doi: 10.1029/2019JB018285.
599
600 Hanawa, K., & Mitsudera, F. (1985), On the data processings of daily mean values of
601 oceanographical data: Note on the daily mean sea-level data. *Bulletin on Coastal Oceanography,*
602 *23*(1), 79-87. doi: 10.32142/engankaiyo.23.1_79.

Hasegawa, T., Nagano, A., Ariyoshi, K., Miyama, T., Matsumoto, H., Iwase, R., & Wakita, M. (2021), Effect of ocean fluid changes on pressure on the seafloor: Ocean assimilation data analysis on warm-core rings off the southeastern coast of Hokkaido, Japan on an interannual timescale. *Frontiers in Earth Science: Solid Earth Geophysics, 9*, 600930. doi: 10.3389/feart.2021.600930.

Hasegawa, T., Nagano, A., Matsumoto, H., Ariyoshi, K., & Wakita, M. (2019), El Niño-related sea surface elevation and ocean bottom pressure enhancement associated with the retreat of the Oyashio southeast of Hokkaido, Japan. *Marine Geophysical Research, 40*, 505-512. doi: 10.1007/s11001-019-09392-8.

Hino, R., Inazu, D., Ohta, Y., Ito, Y., Suzuki, S., Iinuma, T., et al. (2014), Was the 2011 Tohoku-Oki earthquake preceded by aseismic preslip? Examination of seafloor vertical deformation data near the epicenter. *Marine Geophysical Research, 35*(3), 181-190. doi: 10.1007/s11001-013-9208-2.

Hirose, F., Nakajima, J., & Hasegawa, A. (2008), Three-dimensional seismic velocity structure and configuration of the Philippine Sea slab in southwestern Japan estimated by double-difference tomography. *Journal of Geophysical Research: Solid Earth, 113*(B9), B09315. doi: 10.1029/2007JB005274.

625 Ide, S., Beroza, G. C., Shelly, D. R., & Uchide, T. (2007), A scaling law for slow earthquakes.
626 *Nature, 447*(7140), 76-79. doi: 10.1038/nature05780.
627
628 Iinuma, T., Hino, R., Kido, M., Inazu, D., Osada, Y., Ito, Y., et al. (2012), Coseismic slip
629 distribution of the 2011 off the Pacific Coast of Tohoku earthquake (M9.0) refined by means of
630 seafloor geodetic data. *Journal of Geophysical Research: Solid Earth, 117*(B7), B07409. doi:
631 10.1029/2012JB009186.
632
633 Inazu, D., Hino, R., & Fujimoto, H. (2012), A global barotropic ocean model driven by synoptic
634 atmospheric disturbances for detecting seafloor vertical displacements from in situ ocean bottom
635 pressure measurements. *Marine Geophysical Research, 33*(2), 127-148. doi: 10.1007/s11001-
636 012-9151-7.
637
638 Inoue, T., Ito, Y., Wallace, L. M., Yoshikawa, Y., Inazu, D., Garcia, E. S. M., et al. (2021),
639 Water depth dependence of long-range correlation in nontidal variations in seafloor pressure.
640 *Geophysical Research Letters, 48*(8), e2020GL092173. doi: 10.1029/2020GL092173.
641
642 Ito, Y., Hino, R., Kido, M., Fujimoto, H., Osada, Y., Inazu, D., et al. (2013), Episodic slow slip
643 events in the Japan subduction zone before the 2011 Tohoku-Oki earthquake. *Tectonophysics,*
644 *600*, 14-26, doi: 10.1016/j.tecto.2012.08.022.
645

646 Iwasaki, T., Sato, H., Shinohara, M., Ishiyama, T., & Hashima, A. (2015), Fundamental structure
647 model of island arcs and subducted plates in and around Japan. *2015 Fall Meeting, American*
648 *Geophysical Union*, San Francisco, Dec. 14-18, T31B-2878.
649
650 Jolliffe, I. T. (2002), Principal component analysis, second edition. *Springer*, New York.
651
652 Kaneda, Y., Kawaguchi, K., Araki, E., Matsumoto, H., Nakamura, T., Kamiya, S., et al. (2015),
653 Development and application of an advanced ocean floor network system for megathrust
654 earthquakes and tsunamis. *Seafloor Observatories, Springer Praxis Books*, Springer, Berlin,
655 Heidelberg, 643-663. doi: 10.1007/978-3-642-11374-1_25.
656
657 Kawabe, M. (1985), Sea level variations at the Izu Islands and typical stable paths of the
658 Kuroshio. *Journal of the Oceanographic Society of Japan, 41*, 307-326. doi:
659 10.1007/BF02109238.
660
661 Kawaguchi, K., Kaneko, S., Nishida, T., & Komine, T. (2015), Construction of the DONET real-
662 time seafloor observatory for earthquakes and tsunami monitoring. *Seafloor Observatories,*
663 *Springer Praxis Books*, Springer, Berlin, Heidelberg, 211-228. doi: 10.1007/978-3-642-11374-
664 1_10.
665
666 Kositsky, A. P., & Avouac, J.-P. (2010), Inverting geodetic time series with a principal
667 component analysis-based inversion method. *Journal of Geophysical Research: Solid Earth,*
668 *115*(B3), B03401. doi: 10.1029/2009JB006535.

669

670 Kubota, T., Saito, T., Fukao, Y., Sugioka, H., Ito, A., Tonegawa, T., et al. (2021), Earthquake
671 rupture and tsunami generation of the 2015 M_W5.9 Bonin event revealed by in situ pressure
672 gauge array observations and integrated seismic and tsunami wave simulation. *Geophysical*
673 *Research Letters, 48*(22), e2021GL095915. doi: 10.1029/2021GL095915.

674

675 Kundu, P. K., Allen, J. S., & Smith, R. L. (1975), Modal decomposition of the velocity field near
676 the Oregon coast. *Journal of Physical Oceanography, 5*(4), 683-704. doi: 10.1175/1520-
677 0485(1975)005<0683:MDOTVF>2.0.CO;2.

678

679 Kutzbach, J. E. (1967), Empirical eigenvectors of sea-level pressure, surface temperature and
680 precipitation complexes over North America. *Journal of Applied Meteorology and Climatology,*
681 *6*(5), 791-802. doi: 10.1175/1520-0450(1967)006<0791:EEOSLP>2.0.CO;2.

682

683 Matsumoto, H., & Araki, E. (2021), Drift characteristics of DONET pressure sensors determined
684 from in-situ and experimental measurements. *Frontiers in Earth Sciences: Solid Earth Physics,*
685 *8*: 600966. doi: 10.3389/feart.2020.600966.

686

687 Menemenlis, D., Campin, J.-M., Heimbach, P., Hill, C., Lee, T., Nguyen, A., et al. (2008),
688 ECCO2: high resolution global ocean and sea ice data synthesis. *Mercator Ocean Quarterly*
689 *Newsletter, 31*, 13-21.

690

691 Munekane, H. (2012), Coseismic and early postseismic slips associated with the 2011 off the
692 Pacific coast of Tohoku Earthquake sequence: EOF analysis of GPS kinematic time series.
693 *Earth, Planets and Space, 64*(12), 3. doi: 10.5047/eps.2012.07.009.
694
695 Muramoto, T., Ito, Y., Inazu, D., Wallace, L. M., Hino, R., Suzuki, S., et al. (2019), Seafloor
696 crustal deformation on ocean bottom pressure records with nontidal variability corrections:
697 Application to Hikurangi Margin, New Zealand. *Geophysical Research Letters, 46*(1), 303-310.
698 doi: 10.1029/2018GL080830.
699
700 Nagano, A., Yamashita, Y., Ariyoshi, K., Hasegawa, T., Matsumoto, H., & Shinohara, M.
701 (2021), Seafloor pressure change excited at the northwest corner of the Shikoku Basin by the
702 formation of the Kuroshio large-meander in September 2017. *Frontiers in Earth Science: Solid*
703 *Earth Physics, 8*, 583481. doi: 10.3389/feart.2020.583481.
704
705 Nagano, A., Yamashita, Y., Hasegawa, T., Ariyoshi, K., Matsumoto, H., & Shinohara, M.
706 (2019), Characteristics of an atypical large-meander path of the Kuroshio current south of Japan
707 formed in September 2017. *Marine Geophysical Research, 40*(4), 525-539. doi: 10.1007/s11001-
708 018-9372-5.
709
710 Nitani, H. (1972), *"Beginning of the Kuroshio", in Kuroshio-its physical aspects*, Editors.
711 Stommel, H., & Yoshida, K., Tokyo, Japan: University of Tokyo Press, 129-163.
712

713 Nuryanto, D. E. (2016), A complex empirical orthogonal function for combining two different
714 variables over Indonesian maritime continent. *AIP Conference Proceedings, 1707*, 050012. doi:
715 10.1063/1.4940844.
716
717 Obara, K., & Kato, A. (2016), Connecting slow earthquakes to huge earthquakes. *Science,*
718 *353*(6296), 253-257. doi: 10.1126/science.aaf1512.
719
720 Ohta, Y., Hino, R., Inazu, D., Ohzono, M., Ito, Y., Mishima, M., et al. (2012), Geodetic
721 constraints on afterslip characteristics following the March 9, 2011, Snariku-oki earthquake,
722 Japan. *Geophysical Research Letters, 39*(16), L16304. doi: 10.1029/2012GL052430.
723
724 Okada, Y. (1992), Internal deformation due to shear and tensile faults in a half-space. *Bulletin of*
725 *the Seismological Society of America, 75*(4), 1135-1154. doi: 10.1785/BSSA0820021018.
726
727 Okada, Y., Nishimura, T., Tabei, T., Matsushima, T., & Hirose, H. (2022), Development of a
728 detection method for short-term slow slip events using GNSS data and its application to the
729 Nankai subduction zone. *Earth, Planets and Space, 74*(1), 18. doi: 10.1186/s40623-022-01576-8.
730
731 Polster, A., Fabian, M., & Villinger, H. (2009), Effective resolution and drift of Paroscientific
732 pressure sensors derived from long-term seafloor measurements. *Geochemistry, Geophysics,*
733 *Geosystems, 10*(8), Q08008. doi: 10.1029/2009GC002532.
734

735 Rouset, B., Campillo, M., Lasserre, C., Frank, W. B., Cotte, N., Walpersdorf, A., et al. (2017), A
736 geodetic matched filter search for slow slip with application to the Mexico subduction zone.
737 *Journal of Geophysical Research: Solid Earth, 122*(12), 10,498-10,514. doi:
738 10.1002/2017JB014448.
739
740 Sato, T., Hasegawa, S., Kono, A., Shiobara, H., Yagi, T., Yamada, T., et al. (2017), Detection of
741 vertical motion during a slow-slip evento off the Boso Peninsula, Japan, by ocean bottom
742 pressure gauges. *Geophysical Research Letters, 44*(6), 2710-2715. doi: 10.1002/2017GL072838.
743
744 Sekine, S., Hirose, H., & Obara, K. (2010), Along-strike variations in short-term slow slip events
745 in the southwest Japan subduction zone. *Journal of Geophysical Research: Solid Earth, 115*(B9),
746 B00A27. doi: 10.1029/2008JB006059.
747
748 Suito, H. (2016), Detectability of interplate fault slip around Japan, based on GEONET daily
749 solution F3. *Journal of the Geodetic Society of Japan, 62*(3), 109-120. doi:
750 10.11366/sokuchi.62.109. [In Japanese]
751
752 Suzuki, K., Nakano, M., Takahashi, N., Hori, T., Kamiya, S., Araki, E., et al. (2016),
753 Synchronous changes in the seismicity rate and ocean-bottom hydrostatic pressures along the
754 Nankai trough: A possible slow slip event detected by the Dense Oceanfloor Network system for
755 Earthquakes and Tsunamis (DONET). *Tectonophysics, 680*, 90-98. doi:
756 10.1016/j.tecto.2016.05.012.
757

758 Takagi, R., Uchida, N., & Obara, K. (2019), Along-strike variation and migration of long-term
759 slow slip events in the western Nankai subduction zone, Japan. *Journal of Geophysical*
760 *Research: Solid Earth, 124*(4), 3853-3880. doi: 10.1029/2018JB018037.
761
762 Tamura, Y., Sato, T., Ooe, M., & Ishiguro, M. (1991), A procedure for tidal analysis with a
763 Bayesian information criterion. *Geophysical Journal International, 104*(3), 507-516. doi:
764 10.1111/j.1365-246X.1991.tb05697.x.
765
766 Thompson, R. O. R. Y. (1983), Low-pass filters to suppress inertial and tidal frequencies.
767 *Journal of Physical Oceanography, 13*(6), 1077-1083. doi: 10.1175/1520-
768 0485(1983)013<1077:LPFTSI>2.0.CO;2.
769
770 Thomson, R. E., & Emery, W. J. (2014), *Data analysis methods in physical oceanography*.
771 Amsterdam: Elsevier B. V. Retrieved from doi: 10.1016/C2010-0-66362-0.
772
773 Tsushima, H., Hino, R., Tanioka, Y., Imamura, F., & Fujimoto, H. (2012), Tsunami waveform
774 inversion incorporating permanent seafloor deformation and its application to tsunami
775 forecasting. *Journal of Geophysical Research: Solid Earth, 117*(B3), B03311. doi:
776 10.1029/2011JB008877.
777
778 Wallace, L. M., Webb, S. C., Ito, Y., Mochizuki, K., Hino, R., Henrys, S., et al. (2016), Slow slip
779 near the trench at the Hikurangi subduction zone, New Zealand. *Science, 352*(6286), 701-704.
780 doi: 10.1126/science.aaf2349.

781

782 Watts, D. R., & Kontoyiannis, H. (1991), Deep-ocean bottom pressure measurement: Drift
783 removal and performance. *Journal of Atmospheric and Oceanic Technology, 7*(2), 296-306. doi:
784 10.1175/1502-0426(1990)007<0296:DOBPMD>2.0.CO;2.

785

786 Watts, D. R., Wei, M., Tracey, K. L., Donohue, K. A., & He, B. (2021), Seafloor geodetic
787 pressure measurements to detect shallow slow slip events: Methods to remove contributions from
788 ocean water. *Journal of Geophysical Research: Solid Earth, 126*(4), e2020JB020065. doi:
789 10.1029/2020JB020065.

790

791 Wells, D. L., & Coppersmith, K. J. (1994), New empirical relations among magnitude, rupture
792 length, rupture width, rupture area, and surface displacement. *Bulletin of the Seismological*
793 *Society of America, 84*(4), 974-1002. doi: 10.1785/BSSA0840040974.

794

795 Wessel, P., Smith, W. H. F., Scharroo, R., Luis, J., & Wobbe, F. (2013), Generic mapping tools:
796 improved version released. *EOS Transactions, 94*(45), 409-410. doi: 10.1002/2013EO450001.

797

798 Woods, K., Webb, S. C., Wallace, L. M., Ito, Y., Collins, C., Palmer, N., et al. (2022), Using
799 seafloor geodesy to detect vertical deformation at the Hikurangi subduction zone: Insights from
800 self-calibrating pressure sensors and ocean general circulation models. *Journal of Geophysical*
801 *Research: Solid Earth, 127*(11), e2022JB023989. doi: 10.1029/2022JB023989

802

803 Yokota, Y., & Ishikawa, T. (2020), Shallow slow slip events along the Nankai Trough detected
804 by GNSS-A. Science Advances, 6(3), eaay5786. doi: 10.1126/sciadv.aay5786.
805

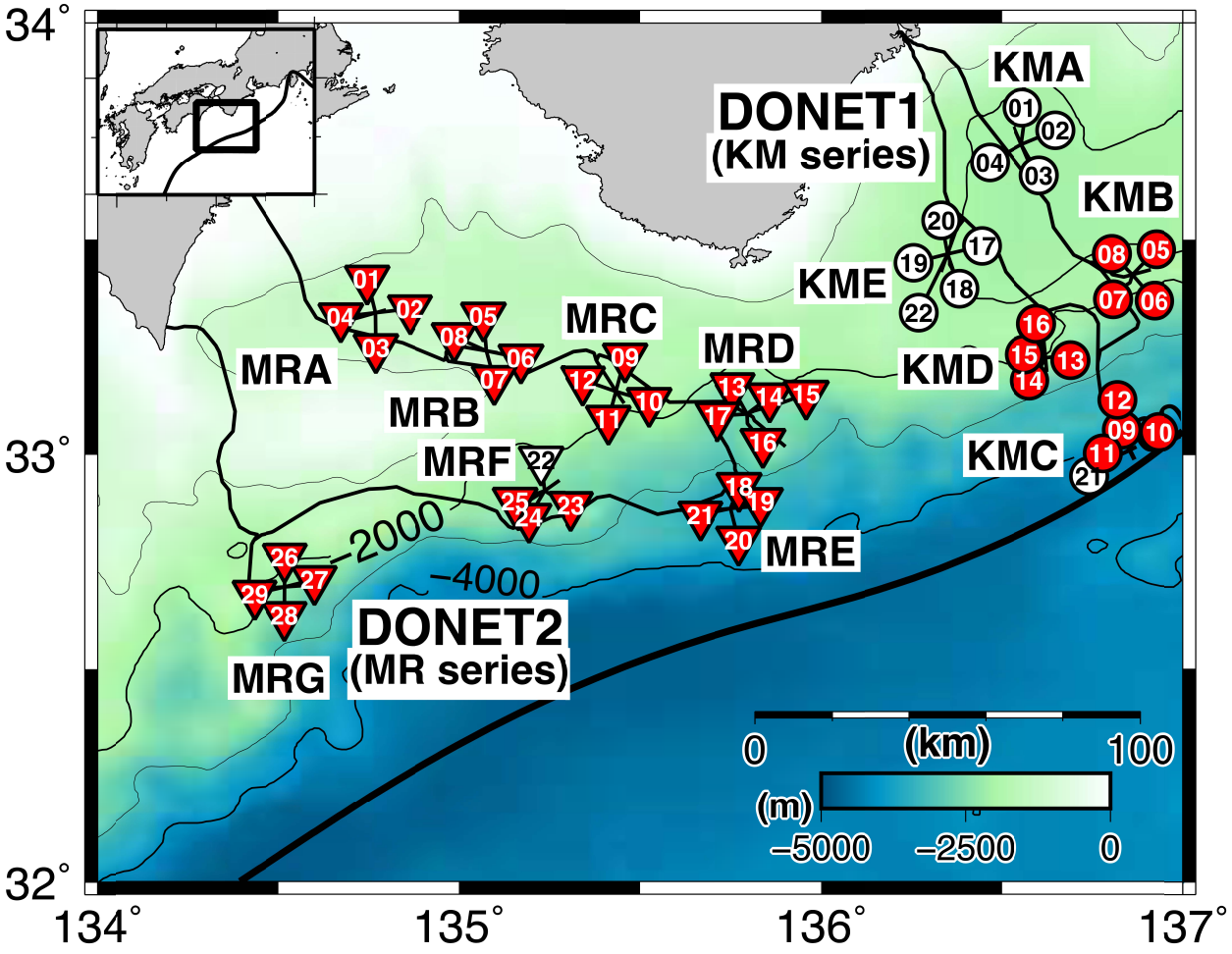

806

807 **Figure 1.** DONET observatory site map. Circles and triangles indicate the DONET1 and DONET2
808 observation sites, respectively. A group of four or five observation sites is a "node," and the node name is
809 shown in the vicinity of each node. For example, the name of the westernmost site is MRG29. The red-
810 colored sites are used for our principal component analysis. The bold black line indicates the Nankai
811 trough (Iwasaki et al., 2015).
812

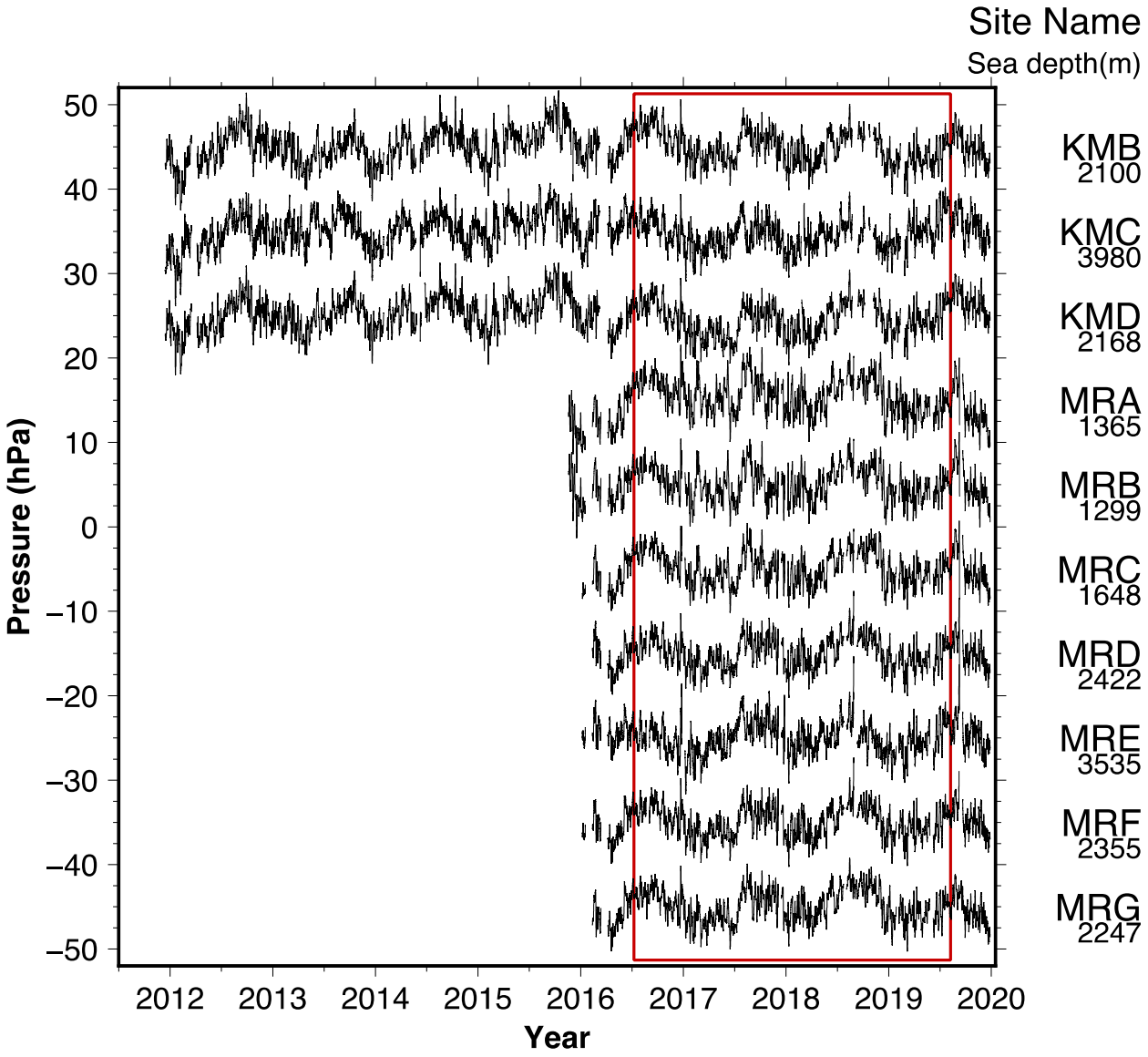

Figure 2. An averaged 8-year long-term continuous OBP time series for each node. The red rectangle indicates the analysis period in this study. The node name and the average sea depth of each nodes are shown on the right side of the figure.

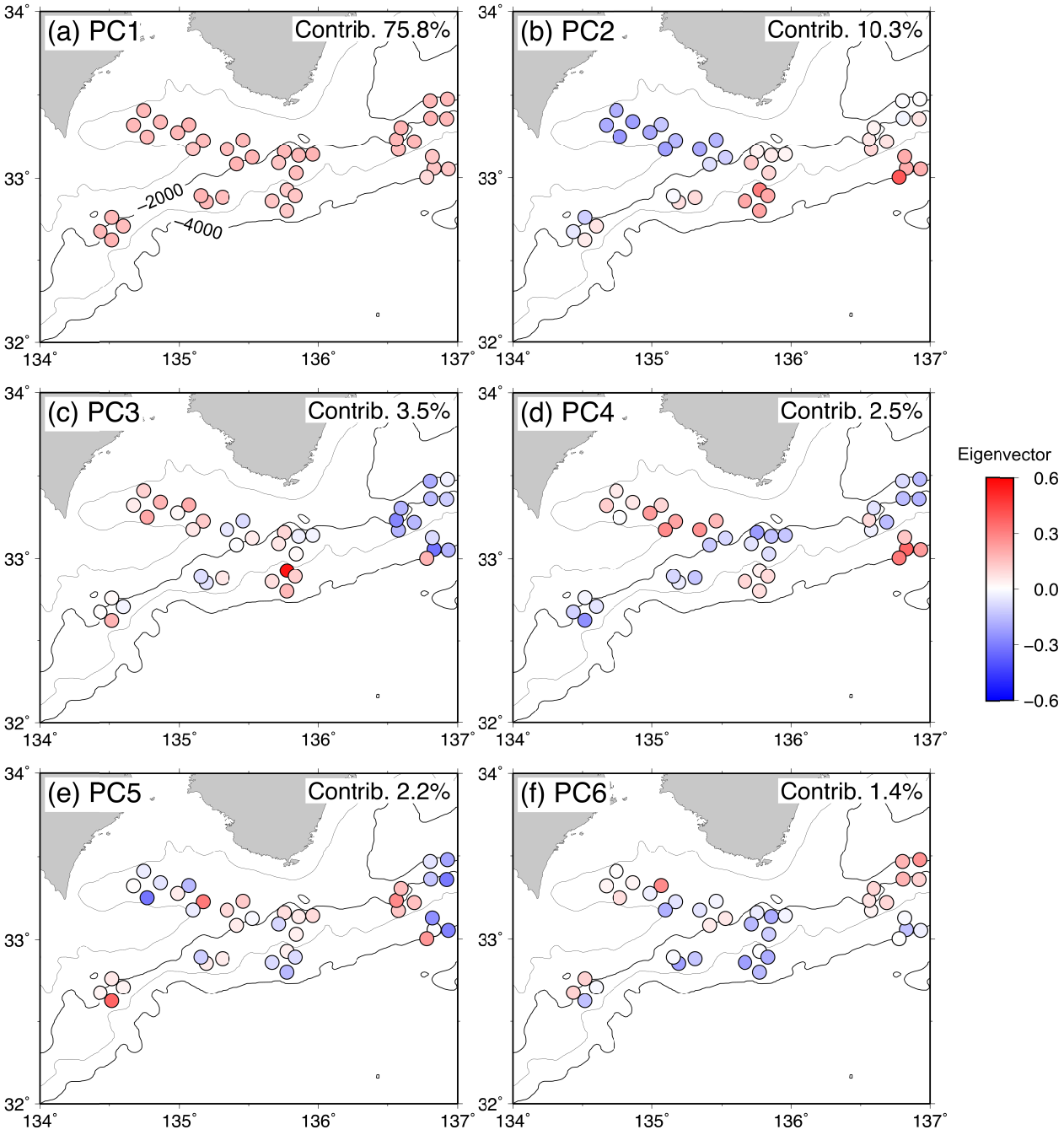

821
822 **Figure 3. (a)** Spatial variation of the PC1 calculated by PCA. **(b)** Same as **(a)**, but for PC2. **(c)** Same as
823 **(a)**, but for PC3. **(d)** Same as **(a)**, but for PC4. **(e)** Same as **(a)**, but for PC5. **(f)** Same as **(a)**, but for PC6.
824 The contribution of each PC is shown in the right-top of the figure.
825

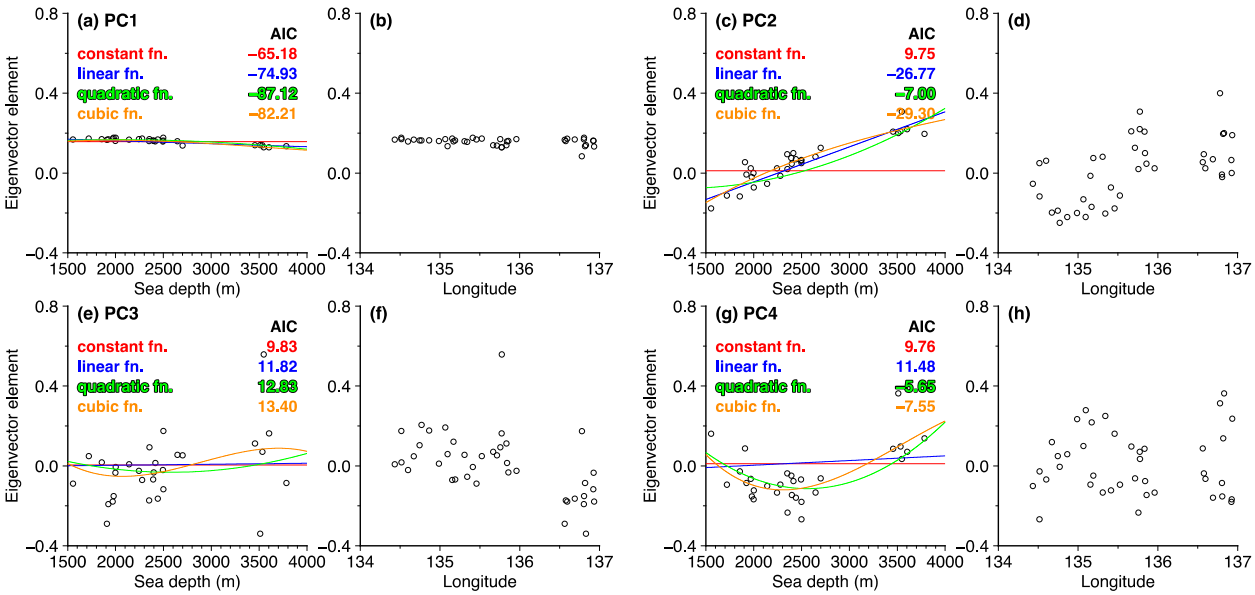

826

827 **Figure 4.** The PC1 variation along with **(a)** sea depth or **(b)** longitude. **(c, d)** Same as **(a, b)** but for PC2.
828 **(e, f)** Same as **(a, b)** but for PC3. **(g, h)** Same as **(a, b)** but for PC4. The red, blue, green, and orange lines
829 indicate the approximations using a constant function, a linear function, a quadratic function, and a cubic
830 function, respectively. The AIC (Akaike, 1973) rates of each approximation are shown in the top right
831 figure in **(a)**, **(c)**, **(e)**, and **(g)**.
832

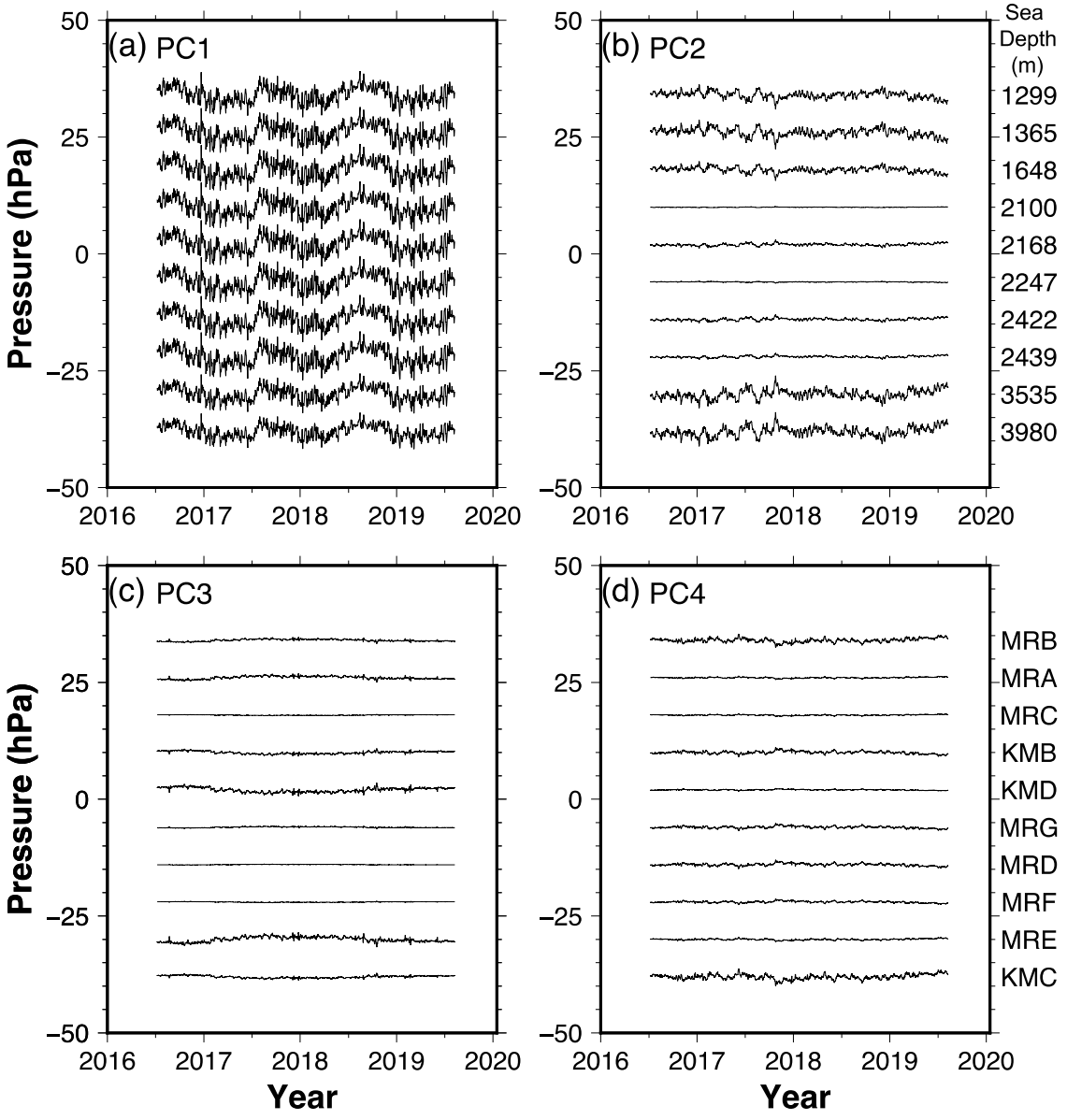

Figure 5. Each principal component time series sorted by sea-depth. The time series for **(a)** PC1, **(b)** PC2, **(c)** PC3, and **(d)** PC4. The rough sea depths and the station names are shown in the right side of **(a)** and **(d)**, respectively. The time series for each station are referenced in Figure S13.

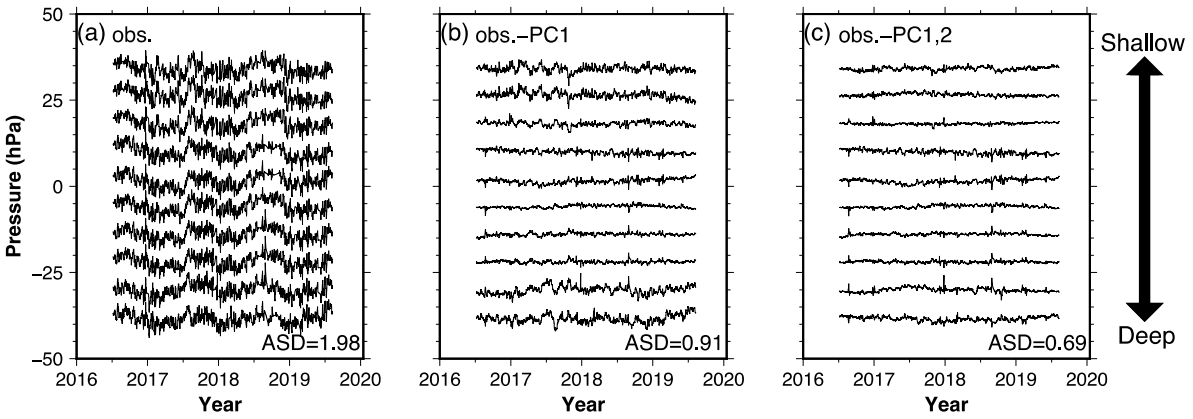

Figure 6. OBP time series for each node with offset sorted by sea depth for **(a)** the observations, **(b)** after removing PC1, and **(c)** after removing PC1 and PC2. The averaged standard deviation (ASD) of each process is **(a)** 1.98, **(b)** 0.91, and **(c)** 0.69. The beards in the time series are caused by the interpolation of the missing period. The time series for each station are referenced in Figure S14.

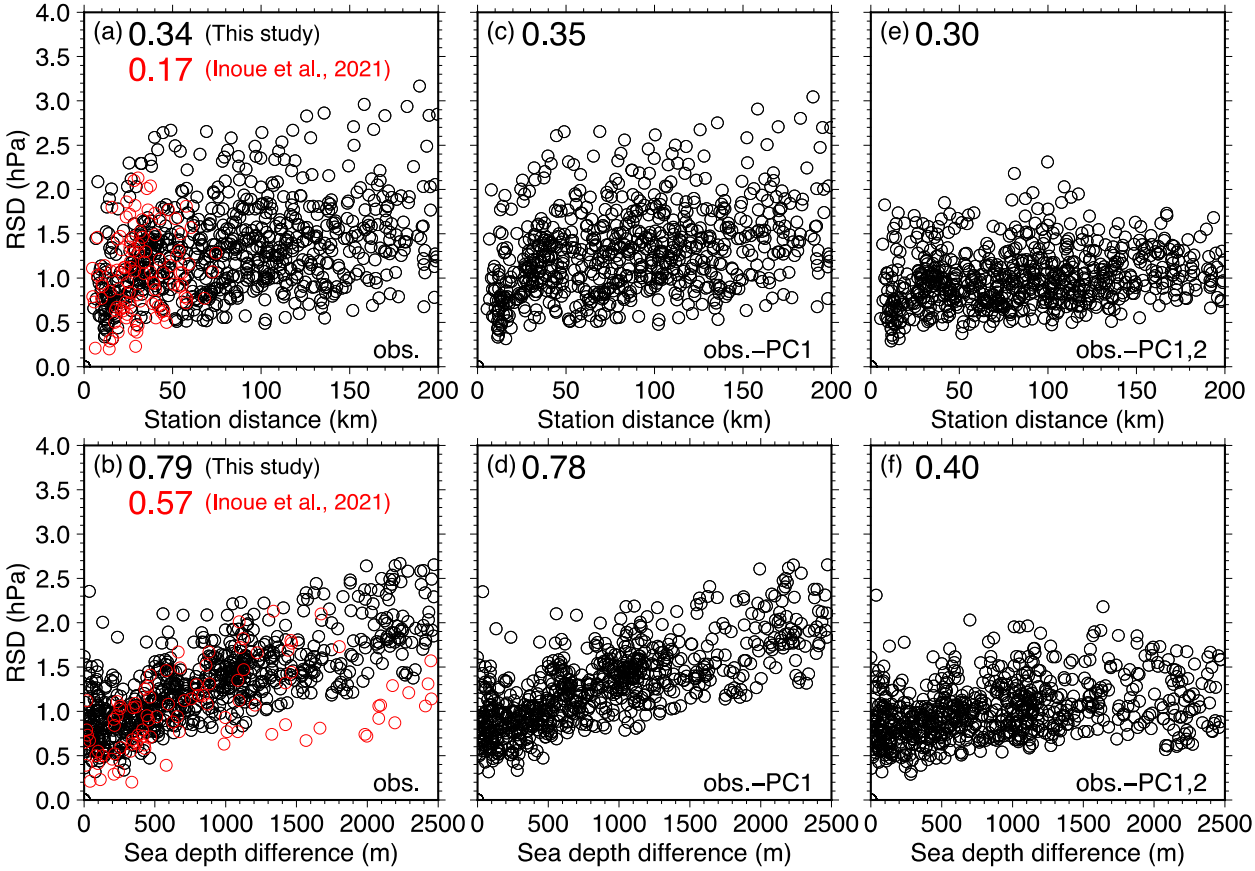

Figure 7. The correlation distribution between the standard deviation of the relative pressure time series (RSD) and the station distance **(a, c, e, g)** or the sea-depth difference **(b, d, f, h)**. The standard deviation is calculated for **(a, b)** the observation, **(c, d)** after removing PC1, and **(e, f)** after removing PC1 and PC2. Black dots indicate the correlation between the standard deviation and the distance or the sea-depth for each relative pressure time series. Red dots indicate the same thing as the black dots but for the off-Hikurangi margin (Inoue et al., 2021). The upper number is the correlation coefficient between the two axes for each figure.

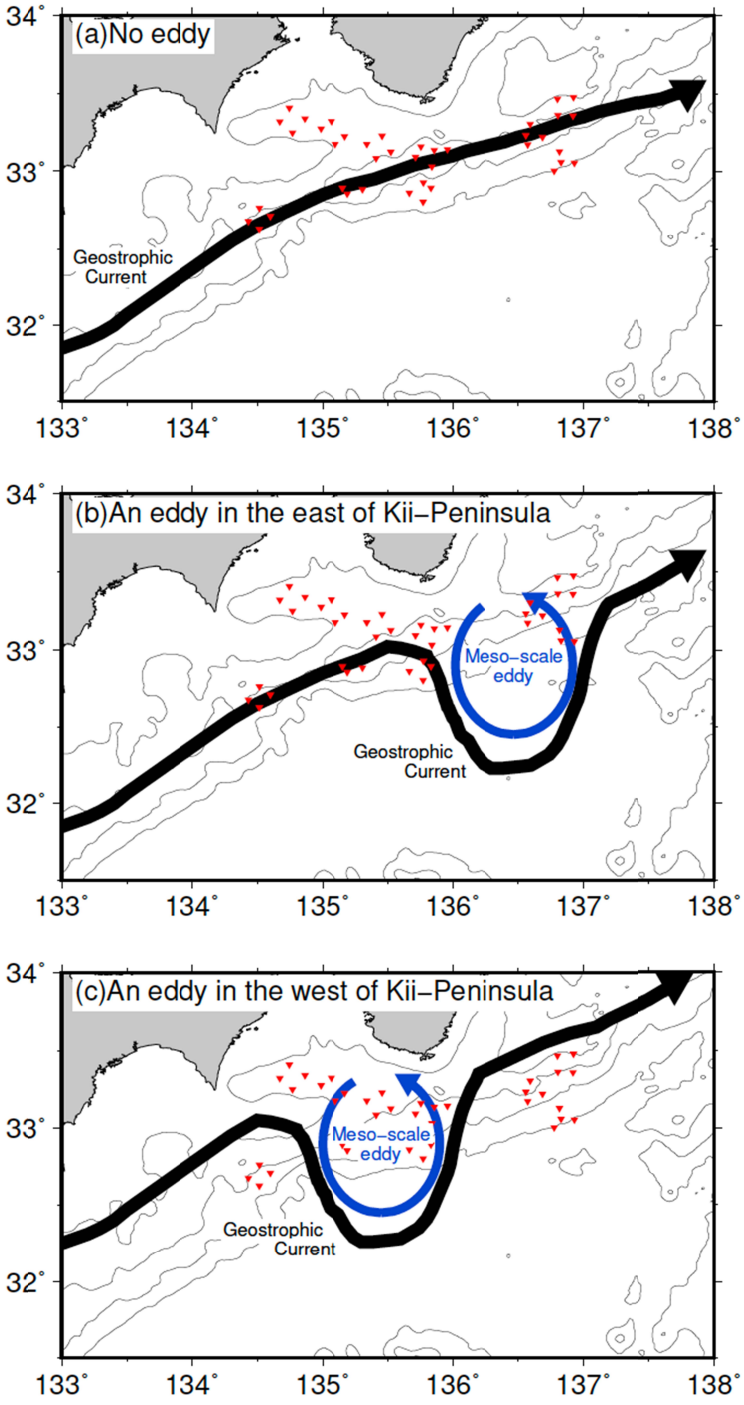

Figure 8. The sketches on the interpretation of the spatial distribution of each principal component. **(a)** The geostrophic current (Kuroshio Current) without meandering and eddy. **(b/c)** The geostrophic current with a mesoscale eddy (cold vortex) located in the south east/west of Kii-Peninsula. Black bold arrow indicates the flow path of the geostrophic current. Blue arrow indicates the image of the meso-scale eddy corresponding to the geostrophic current. Red triangles indicate the DONET observation points used in this study.

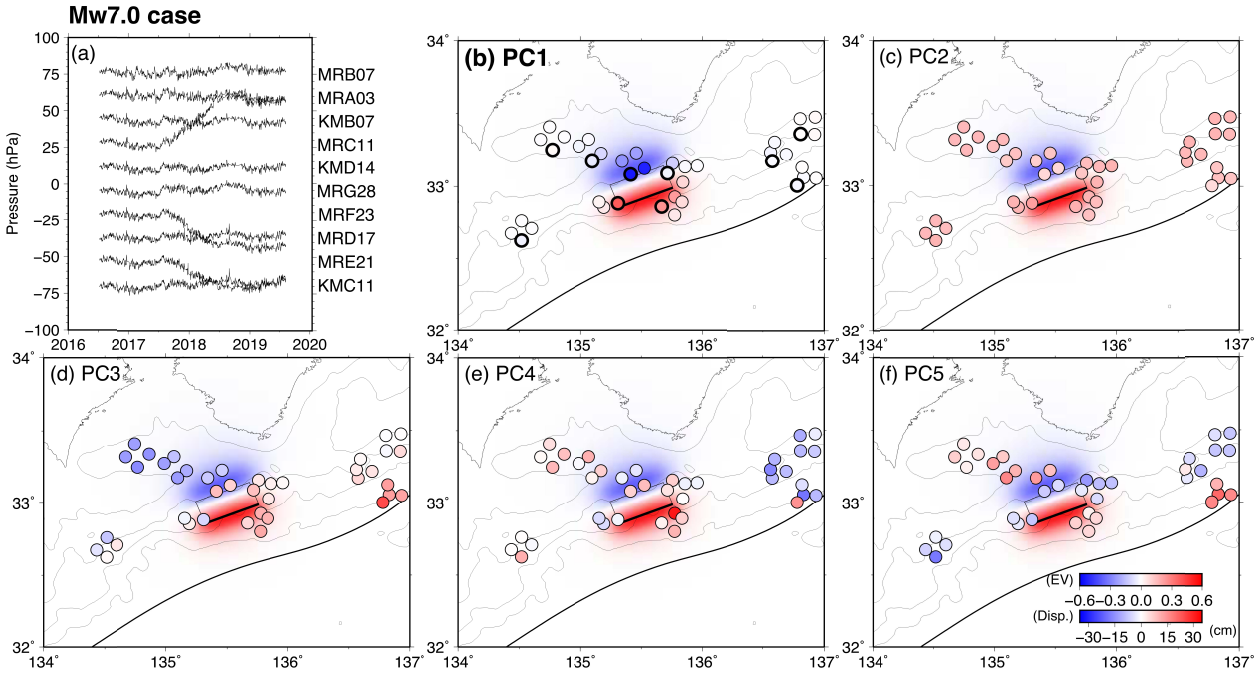

Figure 9. Time series and spatial distribution of PCA assuming a synthetic rectangular fault model of M_W7.0 centered at 135.5°E, 33.0°N. Figures with bold captions reflect the assumed synthetic ramp (In this case, **(b)** reflects the synthetic ramp.) **(a)** The pressure time series representing each node after applying a synthetic ramp to the observed time series (Figure 6(a)). **(b)** Spatial distribution of the PC1 when PCA is applied to the time series in **(a)**. The bold circles indicate the observation sites whose time series are illustrated in **(a)**. **(c–f)** Same as **(b)**, but for PC2, PC3, PC4, and PC5, respectively. The rectangular area indicates the assumed fault model, and the background color shows the vertical displacement calculated from the synthetic fault model. The thin line indicates the isobath with the interval of 1000m.

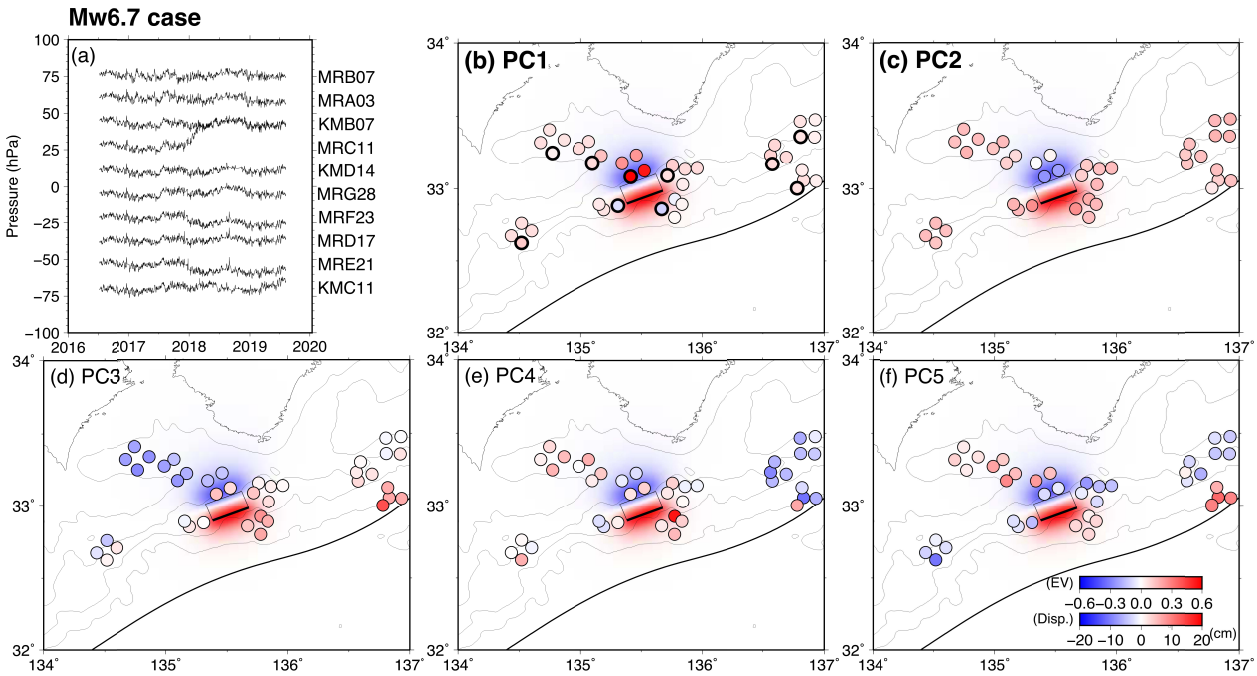

Figure 10. The views of the figures are the same as in Figure 9, but for the Mw6.7 case. In this case, **(a)** and **(b)** reflect the synthetic ramp.

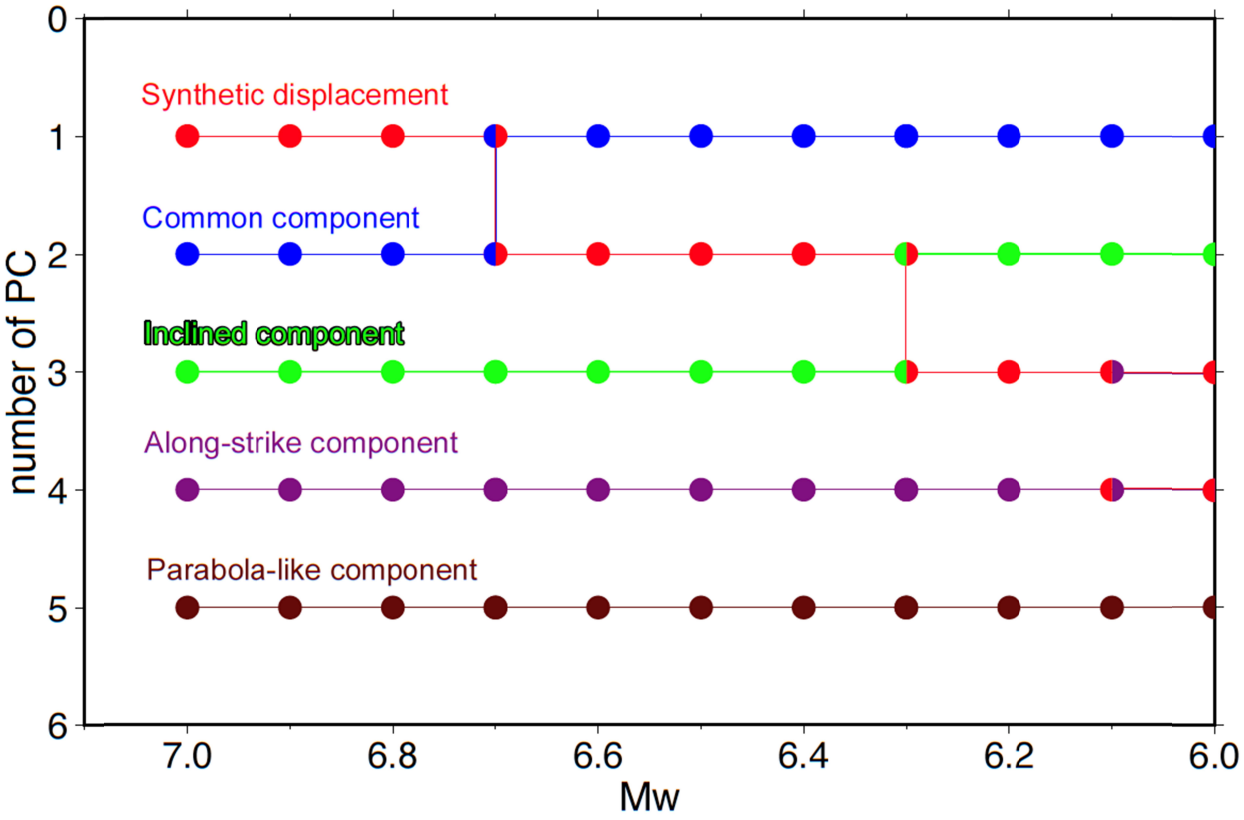

Figure 11. The PC variation per Mw based on the spatial distribution of each PC by the synthetic fault centered at 135.5°E, 33.0°N. As the Mw decreases, the applied synthetic displacement component migrates to higher-order PCs. In the Mw6.7 and Mw6.3 cases, the spatial distribution characteristics of PC1 and PC2 or PC2 and PC3, respectively, are mixed.

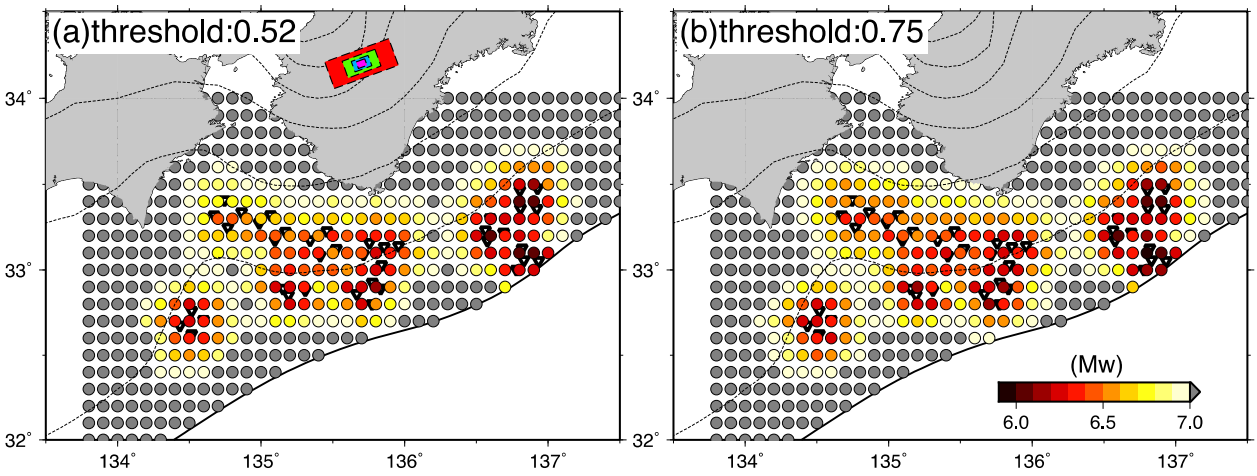

Figure 12. (a) The lower limit of the detectable Mw for each center position of the synthetic rectangular fault using only OBP data and PCA for the threshold of 0.52. **(b)** Same as **(a)**, but for the threshold of 0.75. The rectangles with dotted lines indicate the case of Mw7.0 (red), Mw6.5 (green), Mw6.0 (light blue), and Mw5.5 (pink).

Table 1. The duration, length, and slip of rectangular fault calculated by Wells & Coppersmith (1994) and Equation (3) for each moment magnitude.

Mw	Duration (days)	Length (km)	Slip (cm)	Mw	Duration (days)	Length (km)	Slip (cm)
5.5	1.6	5.9	28.7	6.3	25.9	17.1	73.4
5.6	2.3	6.7	32.3	6.4	36.6	19.6	82.6
5.7	3.3	7.7	36.3	6.5	51.7	22.4	92.9
5.8	4.6	8.8	40.8	6.6	73.0	25.6	104.4
5.9	6.5	10.0	45.9	6.7	103.2	29.2	117.5
6.0	9.2	11.5	51.6	6.8	145.7	33.4	132.1
6.1	13.0	13.1	58.1	6.9	205.8	38.2	148.6
6.2	18.3	15.0	65.3	7.0	290.7	43.7	167.1

Table 2. Normalized Inner Product (NIP) between the two PC2s for each moment magnitude assuming a rectangular fault at 135.5°E, 33.0°N. The spatial distribution of each PC2 is shown in Figure S11.

Mw	NIP
5.5	1.00
5.6	1.00
5.7	1.00
5.8	1.00
5.9	1.00
6.0	1.00
6.1	1.00
6.2	0.99
6.3	0.78
6.4	0.40
6.5	0.32
6.6	0.30
6.7	0.21
6.8	0.12
6.9	0.09
7.0	0.07